Dynamic Behaviour and Catenary Action of Axially-restrained Steel Beam Under Impact Loading

**Jingsi Huo[a,b]; Jinqing Zhang [b]; Yanzhi Liu [b]; Feng Fu[c]

[a]College of Civil Engineering, Huaqiao University, 361021, Xiamen, China.
[b]China Ministry of Education Key Laboratory of Building Safety and Energy Efficiency, College of Civil Engineering, Hunan University, Yuelu Mountain, Changsha, 410082, China
[c]School of Engineering and Mathematical Sciences, City University London, Northampton Square, London, EC1V 0HB

Abstract: In this paper, the dynamic behaviour and catenary action of axially restrained steel beam under impact loadings is examined through a combination of experimental and numerical investigations. It describes and discusses the results of six impact tests on the axially restrained welded H-beams by means of the drop hammer test machine. The main behavioural patterns and the key response characteristics including the development of impact force, deformation and strain, as well as failure modes are examined, with emphasis on the effect of impact energy and the width to thickness ratio of beam flange. Finite element models are also developed and validated against the available testing results. It is demonstrated that the detailed FE model can capture the response of the welded H-beams under impact loadings. Moreover, the mechanism of catenary action was identified based on the development of the internal force in the welded H-beams.

Keywords: restrained steel beam; impact test; finite element simulation; catenary action

** Please address all correspondence to Professor Jingsi Huo, Tel: 86 592 6162698, Fax: 86 592 6162698, E-mail: jingsihuo@gmail.com.

1. Introduction

Along with the development of high-rise buildings and long span structures, designers and researchers pay more and more attention to structure's progressive collapse caused by the extreme loading such as blast, impact and earthquake action. Based on the investigation of the collapse mechanism due to the terrorist attack, various design guidance has been proposed in many countries. The main mitigating method in these design guidance is suggested to provide redundant alternative path for force transfer [1], while some other approaches are proposed to utilize the catenary actions [2-4]. However, the resistance to the progressive collapse of frame structure is not clear. The way to utilize the catenary action is still needed to be studied experimentally and numerically. Some researchers [5-7] performed non-linear finite element modeling for frame structures and investigated their capacities under the event of progressive collapse. Simplified methods was also proposed to strengthen the structure and mitigate the development of progressive collapse [8-9].

In the idealized situations of progressive collapse, the effect of the sudden removal of a column is similar to the instantaneous application of gravity loads to the floor system. In such a case, connections within the removed column zone could be subjected to significant bending moment as well as tensile force. Gradually, the force mechanism changes into pure tension, which is so-called catenary actions. This is a resisting mechanism, which allows the beam to carry vertical loads at large displacements even if

the ultimate bending state has been reached in the critical sections. In catenary action, elements (e.g., beams and slabs) that are intended to support flexural loadings undergo large deformation and have sufficiently stiff and strong anchorages to take on load as tension members [10]. Kim et al [10] applied non-linear static and dynamic analysis method to study the advantage of catenary action in resisting progressive collapse of framed buildings. It was found that in the development of the catenary action, the bending moment of the connection reduced, while axial force arise gradually with the vertical displacement increasing.

Many experimental studies and finite element simulations have been performed on the catenary effect [11-16]. Liu et al [11,12] studied the behaviour of the catenary action in the beam after the loss of the column. It was concluded that the catenary action can reduce the bending moment of the beam and effectively resist the progressive collapse of the structure. He et al [13] carried out experimental studies on concrete frame to investigate the catenary effect. Testing results stated that the arch action and the catenary action were formed consecutively. It is also pointed out that the maximum deformation capacity and tensile capacity are two key factors in resisting the progressive collapse. Sadek et al [14] also investigated the performance of steel and reinforced concrete beam-column connection under monotonic vertical displacement of a center column through an experimental and computational assessment. Huo et al [15] performed impact testing on the hot-rolled H-shaped beam with restrains at its two ends.

The development of the internal force and the catenary action during the impact testing were deeply studied. Recently, Li et al [16] examined the catenary behaviour of welded unreinforced flange bolted web connections under static pushing-down column displacement by means of full-scale testing and numerical simulation. The bolted connections have shown robust in withstanding large deformations whilst the resistance mechanism transitioned to a catenary action phase.

It can be noted from the above literature review that catenary action plays an important role in resisting the progressive collapse of the frame. However, most of the research concentrated on the performance of catenary action under static loading conditions. There is also a clear need for experimental investigation to examine the structure's dynamic behaviour and characterize the mechanism of catenary action. Therefore, this paper deals with the dynamic behaviour and catenary action of axially restrained steel beam under impact loadings through a combination of experimental and numerical investigations. It describes and discusses the results of six impact tests on the axially restrained welded H-beams by means of the drop hammer test machine. The main behavioural patterns and the key response characteristics including the development of impact force, deformation and strain, as well as failure modes are examined, with emphasis on the effect of the width to thickness ratio of beam flange and impact energy. Finite element models are developed and validated against the available testing data. Moreover, the mechanism of catenary action was identified based on the development

of the internal force in the welded H-beams.

2. Experimental programme

2.1 Testing set-up and specimen details

Six impact tests on the axially restrained welded H-beams were carried out by means of the drop hammer test machine at the Center for Integrated Protection Research of Engineering Structures (CIPRES) in Hunan University. The testing set-up is depicted in Fig. 1, where a drop hammer impact force was applied at the mid-span of the steel beam, and the beam ends were simplified. The drop hammer test equipment was designed with a maximum drop weight of 980 kg and a maximum drop height of 16 m. The hammer with certain weight was released at a given height, and fell down along the guide rails to impact on the middle section of the steel beams. Meanwhile, a high-frequency data acquisition system was used to record the testing response, including the impact force, beam deflections and strains at a 5 mHz sampling rate. Fig. 2 shows the location for the strain gauges. Nine strain gauges were arranged in the flange and the web of the testing beam. Moreover, a high-speed video camera was employed to capture the beam deformation from the lateral side within a frequency of 1000 times per second.

In accordance to GB50017-2003, Code for Design of Steel Structures[17], the impact zone in the steel beam was strengthened by a 10mm thick plate on the upper flange and 8mm thick web stiffeners at the mid-span, as described in Fig. 2, and the ends of the

beam were also stiffened with side plates to avoid the local buckling and fracture. Since the main investigation in this paper focuses on the effect of width to thickness ratio of the beam flange as well as the impact energy on the progressive collapse resistance of the beam, six testing specimens with different b_f/t_f ratios at different impact loadings were designed followed by the requirement in the code for Design of Steel Structures [17]. The designing details were demonstrated in Huo et al. [15]. The details of the specimens are summarized in Table 1, where HW in the reference stands for welded H shape section, followed by the width to thickness ratio, the weight of the hammer (where the number '4' '5' '7' stands for 450 kg, 575 kg and 700 kg, respectively), as well as the dropping height (where the number '5' '6' '8' '7' stands for 5.0 m, 6.0 m, 8.0 m and 6.5 m, respectively. λ is the width to thickness ratio (b_f/t_f). M and v are the mass of the hammer and the velocity of the hammer, respectively. In addition, as depicted in Table 1, other four impact tests on the hot-rolled H-beams completed by the authors [15] were also drawn into this paper as comparative data, but the details were presented in Huo et al. [15]. In the reference of these four beams, HR stands for hot-rolled H shape section, other items are taken similar to that of welded H-beams.

Furthermore, the corresponding testing results are presented in Table 1, where the impact energy E_1 is obtained from the equation $Mv^2/2$, while E_2 is the energy dissipated by the beams, which can be evaluated by the area below the impact force versus displacement curves. In order to discover the effect of width to thickness ratio on the

dynamic behavior of steel beams under impact loading, the impact energy is normalized by the beam yield moment according to the work by Jones and Shen [18].The normalized impact energy E_1/M_y is also summarized as the ratio between applied impact energy and beam yield moment. $F_{u,max}$ is the ultimate impact force taken as the peak value on the time history curve of impact force. $F_{u,e}$ is the averaged plateau impact force which is evaluated by averaging the impact forces at the starting points of the stable stalemate stage in its time history curve, while $F_{u,c}$ is the predicted quasi-static concentrated force based on the testing strain development in the stable stalemate stage through force balance equation. Whereas, F_p is the plastic capacity of the beam calculated by the equation $F_p=4M_p/l$ (where M_p is the beam plastic bending capacity, and l is the beam span). Herein, the ratio of F_u/F_p (or $F_{u,e}/F_{u,c}$) is defined as the amplification factor (*DAF*), where DAF_1, DAF_2 and DAF_3 are presented in Table 1. $\dot{\varepsilon}$ is the strain rate equal to the maximum stain ε_{max} over time t. The maximum rotation at the mid-span of the beam φ_{max} and the residual rotation φ_u are calculated by the equations $\varphi_{max}=2\delta_{max}/l$ and $\varphi_u=2\delta_u/l$, respectively ($\delta_{max}$is the maximum deflection of the beam, and δ_u is the beam residual deflection).

The beams were all made of Grade Q235 steel. The material properties for the beam flange and web components as obtained from coupon tests are presented in Table 2.

2.2 Testing results and observations

Table 1 summarizes the main response parameters obtained from the impact tests on the axially restrained welded H-beams, while Figures 3-9 present the deformation patterns as well as the impact force and displacement relationships. In subsequent sections, the experimental results and observations from the six welded H-beam specimens are presented and discussed by considering the influence of the width to thickness ratio and impact energy on the beam behaviour.

2.2.1 Deformation mode

Fig. 3 shows the deformation patterns observed for the six testing specimens. It can be observed from Table 1 and Fig. 3 that larger deformation took place when the increasing impact energy was employed. Moreover, due to the higher width to thickness ratio, the local deformation for the welded section is larger than that of the hot-rolled section as described in Huo et al. [15].

Fig. 4 presents the residual deflection shapes of the testing beams in comparison with the corresponding half-sinusoid curves. It can be observed that the deflection curve matched well the corresponding half-sinusoid curve. Importantly, the residual deformation of Specimen HR7-46 is also depicted in Fig. 4 for comparison. It is obvious that the deflection of Specimen HR11-58 is much larger than that of Specimen HR7-46, although the same normalized impact energy E_1/M_y was applied. This can be attributed to the higher width to thickness ratio of the former beam. This can be also

further demonstrated in Fig. 5. It is observed from the normalized impact energy-beam rotation (including the peak and residual rotation at the mid-span) curves that higher normalized impact energy leaded to larger bending deformation, while less rotation took place on the beams with lower width to thickness ratio when the same normalized impact energy was employed.

The development of the plastic deformation for the welded beam under impact force was also recorded by a high speed camera. The captured pictures of the deformation development for Specimen HW14-76 from 0 ms to 32 ms are illustrated in Fig. 6. It is observed that the local deformation of the flange and web occurred together with the beam bending deformation, but the local deformation grew faster and more evident. At the time of 4 ms, some deformation can be observed near the web stiffener, but slight beam global deformation happened. In the next 4-ms step, local buckling occurred at the top flange in the middle beam, while shear deformation was observed at the web near the web stiffener with little global deformation. Afterwards, beam global deformation started to develop rapidly and reached its maximum rotation value at the time of around 24 ms. The beam bending then rebounded as the impact force descended till the end of the testing. These are discussed in more detail in subsequent sections through the impact force and deformation relationships.

2.2.2 Time history of impact force and displacement

The time history curves of impact force as well as the mid-span displacement for six welded H-beams are depicted in Fig. 7 and Fig. 8, respectively. According to their dynamic response in Fig. 7, three stages can be divided in the time history curve of impact force, including the impact stage, stable stalemate stage and the decaying stage. In the first stage, impact force reached to its maximum value in a very short period of time mostly attributed to the presence of inertia force. A fluctuant descending segment then took place as a result of the complex contact condition between the impact hammer and the beam, followed by an about 18 ms platform. The plateau impact force, $F_{u,e}$ as depicted in Tabel 1, was evaluated by averaging the impact forces at the starting points of this platform, which was assumed as the value of impact load without considering the effect of inertia force. And in the final stage, the impact force declined slowly as the impact hammer left from the beam. The similar trend was also described for the hot-rolled beams elsewhere [15,19].

Meanwhile, Fig. 8 illustrates the time history curves of the mid-span displacement for all specimens in correspondence to the impact force-time relationships. Herein four stages were involved in the displacement-time history curves, the elastic deformation, inelastic deformation, constant deformation and rebound deformation. It is observed from Fig. 7 and Fig. 8 that the beam displacement remained elastic in the initial fluctuation, while the plastic displacement developed rapidly when the impact force started to the second wave. As the impact force entered the stable stage, the beam

displacement grew up gently and gradually kept in a short platform. Afterwards, the beam displacement fell down with the impact force decreasing.

Furthermore, it is very important to note from Fig. 7 and Fig. 8 that the influence of the impact energy on the peak impact force and the development of the impact force can be negligible, but the larger impact energy results in higher impact duration and beam deformation. Also, the welded H-beam with larger width to thickness ratio generated lower mid-span displacement subjected to the same applied impact energy in comparison to the specimen with less width to thickness ratio, as illustrated between Specimens HW9-56 and HW11-56 as well as between Specimens HW11-58 and HW 14-58 in Fig. 8. It can be also further confirmed from the definition of normalized impact energy. As depicted in Fig. 5, the ultimate and residual rotation of Specimen HW9-56 was larger than that of Specimen HW11-56, as the normalized impact energy of the former was evaluated higher than the latter when considering the effect of width to thickness ratio. It is also stated that the resistance to the impact loadings of the welded H-beam can be improved with the decreasing width to thickness ratio. But the larger beam flange width led to the relatively obviously local buckling deformation, as depicted in Fig. 3. Correspondingly, the mechanism of catenary action was developed more difficultly for the welded H-section beams with larger width to thickness ratio, in comparison with that for the hot-rolled H-section examined by Huo et al. [15].

2.2.3 Impact force-rotation relationship

The impact force-rotation relationships for six testing beams are shown in Fig. 9, where the beam rotation φ is obtained from the mid-span displacement δ by means of the equation $\varphi=2\delta/l$ (l is the span of the testing beam). Similar to the time history of impact force, the impact force-rotation curves can also be featured as an initial fluctuation and a platform before the rebound of the hammer. In the initial stage, one prompt wave can be observed, but the slope of the descending segment was much less than that of the ascending one. It is indicated that the large rotation occurred on the beam after the peak point. It is also found that in the initial stage the total rotation of the beams with the same section size increased with the higher employed impact energy. In the second stage, the rotation continued to develop. After some relatively gentle fluctuations, the curve came into a plateau. As viewed in Fig. 9, the impact force and the rotation of the beam then started to rebound due to the leave of the hammer from the beam surface.

2.2.4 Analysis of internal force

Fig. 10 presents the time history of strain at the mid-span section for Specimens HW11-56 and HW11-58 under impact, while Fig. 11 summarizes the development of axial strain along the height of the mid-span section for Specimens HW11-56 and HW11-58 during the test according to the strain values at the location of S1, S3, S5, S2, respectively, where η stands for the relative position of the strain along the height of the cross section ($\eta=h'/h$). In addition, due to accident of the data logger system during the testing, the strain of S2 for Specimen HW11-58 was out of work at a time of 10 ms, so

the value of S2 after this moment in Fig. 10(b) makes no sense. It can be seen from Fig. 6 that in initial 1 ms the beam is still in the elastic stage, where the elastic moment M_e can be calculated by $M_e=\sigma \cdot W_x$ (σ can be derived from the mid-section strain through a hardening stress-strain model without considering the strain-rate effect, W_x is the bending modulus of welded H-beam section). Afterwards, the strain at the beam flange increased dramatically to the yield point. But the neutral axis was still kept at the middle of the mid-span section, as indicated in Fig. 11(a) at the rotation of 0.007 rad and 0.020 rad for Specimen HW11-56, and Fig. 11(b) at the rotation of 0.011 rad and 0.025 rad for Specimen HW11-58. As the plastic moment capacity M_p equates to $f_y \cdot W_{xp}$, the yield load F_p can be work out through Equation $F_p=4M_p/l$ based on bending mechanism. This calculation approach takes no consideration on the effect of catenary action, which resulted in lower estimation than the value $F_{u,e}$ obtained from testing data. In the stable stage, S5 increased quickly and S3 changed from compression into tension as observed in Fig. 10. Moreover, Fig. 11 demonstrated that the neutral axis positioned higher at the rotation of 0.045 rad and 0.052 rad for Specimen HW11-56, and 0.057 rad and 0.074 rad for Specimen HW11-58. It can be concluded that axial force developed on the beam at this stage.

Based on the strain values (Gauges S1, S2, S3 and S5) in the mid-section of the beam, the developed moment M and axial force N was integrated through the condition of internal force equivalence. Eventually, the relationship of the moment and axial force at the mid-span section to the rotation for all specimens was obtained as depicted in Fig.

18 in the comparison with the numerical results, which will be further described and discussed in Section 4. Moreover, as the impact force remained plateau in the stable stage, a quasi-static impact force, $F_{u,c}$, was derived from Equation $M_u=(F_u-2N_i\varphi_i)\cdot L/4$ corresponding to the plateau impact force $F_{u,e}$. It is found that herein the predicted concentrated load, $F_{u,c}$, was determined without considering the dynamic loading effect, i.e. the strain-rate effect.

In a whole, the yield load F_p, the impact plateau force $F_{u,e}$ and the predicted concentrated load $F_{u,c}$ are clearly stated in above discussion, and summarized in Table 1. Evidently, the amplification factor DAF_1, $F_{u,c}/F_p$ depicted in Table 1, indicates the effect of the catenary action on the load-carrying capacity of the axially restrained steel beams. It is shown from the amplification factor DAF_1 that the load-carrying capacities was increased by an average of 18% for the welded H-steel beams and 30% for the hot-rolled H-steel beams due to the effect of the catenary action. The amplification factor DAF_2, $F_{u,e}/F_{u,c}$, considers the effect of the dynamic load on the load-carrying capacity of the axially restrained steel beams. The beam load-carrying capacities was increased by an average of 34% for the welded H-steel beams and 40% for the hot-rolled H-steel beams due to dynamic effect and strain hardening. The amplification factor DAF_3, $F_{u,e}/F_p$, is the ratio of the impact loads and the plastic loads based on bending mechanism. In comparison with the static flexural resistance, the anti-impact loads was increased by an average of 60% and 71% for the welded and hot-rolled H-steel beams, respectively. Furthermore, it is clear that the impact resistance of steel

beams was obviously deteriorated with the increase of the ratio of flange width to thickness. It can be attributed to the premature local buckling of beam flange.

3. Numerical assessment

This section describes a detailed finite element model for welded H-beam under impact, as assessing their behaviour based on experimental investigations is a cost-prohibitive and time-consuming task. The proposed continuum finite element models were developed by means of the commercial FE software ABAQUS [20]. The model characteristics are described below. These models are then validated against the experimental results and observations presented above. Particular emphasis is given in the discussion presented below to aspects related to the development of the inner forces and the energy dissipation.

3.1 Finite element modelling

3.1.1 Modelling details

A three-dimensional finite element was developed herein for six impact tests on the axially restrained welded H-beams, as depicted in Fig. 12. The impacted beam as well as the hammer were conducted by means of different elements. It has been pointed out in Reference [21] that beam element cannot accurately simulate the detailed response of the structures, such as the lateral torsional buckling, local buckling, yielding point and

shear stress caused by the blast and fire, and the numerical models with beam elements led to the overestimated resistance of the beam subjected to the impact loading. Therefore, the proposed models in this paper make use of the eight-node brick solid elements of Type C3D8R available in the ABAQUS library [20] to represent the impacted beam and the drop hammer, as shown in Fig. 12. In order to simplify the FE model and improve the convergence, the length of the beam was set as 2500 mm (the distance between hole centers of the tested beam), and the ends of the beam model were strengthened with endplates but without the holes, as shown in Fig.12. Meanwhile, the translational displacement of both beam end sections was constrained, but the rotation was free. A number of mesh sensitivity studies were also carried out in order to arrive at an optimum representation, which involves a comparatively finer mesh for mid-span beam part in contact with the drop hammer and the hammer, whereas a relatively coarser mesh was employed elsewhere.

In addition, as no tearing displacement was observed around the welds during the impact test, welds between the beam flanges and webs as well as those between the beam and stiffeners were modeled by tying together providing an all-freedom coupling of the contact surfaces. Importantly, the contact between the hammer and beam surface was considered by means of explicit ABAQUS contact definitions, named as ‘General contact’, where a ‘hard’ surface contact was defined in the normal direction, while a ‘friction’ surface was employed in the tangential direction with a friction coefficient of

0.2 according to the corresponding research on the dynamic friction factors [22]. The boundary conditions and loading procedure adopted in the numerical analyses replicated those used in the experimental studies described in previous sections. The impact energy was achieved through the application of impact velocity on the hammer with mass definition at the moment that the hammer contact the beam surface.

3.1.2 Material property

The static stress-strain relationships for all the beam components were defined by a bilinear plastic hardening rule with an elastic modulus of 1.80×10^{7} MPa and a poison's ratio of 0.3, as illustrated in Fig. 13. Table 2 provides the static mechanical properties of the beam flange and beam web. However, the true stress and strain in material model were converted from the engineering stress and strain in Table 2 based on Eq. 1 and Eq. 2, respectively. As described in Section 2, the specimens herein suffered from high impact loadings, the strain rate effect was also taken into account in these models. ABAQUS library [20] offers two constitutive models to consider the strain rate effect, the Johnson-Cook model [23] and the Cowper-Symonds model [24]. Herein the Cowper-Symonds model was employed to simulate the strain rate effect. Eq. 3 demonstrates the constitutive equation of Cowper-Symonds model, where σ'_o is the dynamic stress at a uniaxial strain rate $\dot{\varepsilon}$, σ_o is the static stress. D and q are two constants defined for one material. For the mild steel, the value of D and q was generally taken as 40 and 5, respectively, as much research showed that they can give

reasonable agreements with the experimental data [21,25-27]. However, these two values are defined at very small strains [28]. For material under large plastic strains, *D* and *q* are usually evaluated as 6844 and 3.91 [28], respectively. In this paper, the latter was chosen for beam components with severe local buckling under impact.

$$\sigma_{true} = \sigma_{eng}(1 + \varepsilon_{eng}) \tag{1}$$

$$\varepsilon_{true} = \ln(1 + \varepsilon_{true}) \tag{2}$$

$$\frac{\sigma_0'}{\sigma_0} = 1 + \left(\frac{\dot{\varepsilon}}{D}\right)^{1/q} \tag{3}$$

3.2 Validation of FE models

The developed FE model above was employed to simulate the tests from the experimental programme described in Section 2. The comparisons of deformation patterns observed in experimental and numerical models are described for selected specimens in Fig. 14. It is shown that the deformations and plastic mechanisms are replicated by the proposed FE model. Moreover, the experimental and numerical impact force-time relationships as well as impact force-rotation curves are presented in Figs. 15-16, respectively. As demonstrated in Fig. 15, the peak impact force and plateau force, as well as impact period match reasonably well the experimental behaviour for all specimens. In the case of Specimens HW11-56, HW11-58, HW14-58 and HW14-77, minor discrepancies arise in the fluctuant descending segment after the peak point. In

this stage, contact between impact hammer and the beam was complex, which led to the difference for FE model to capture. Furthermore, close correlation is also observed in the impact force- rotation curves from experimental and numerical models as shown in Fig. 16. It is evident from the comparisons that the FE models provide a good prediction of the experimental behaviour in all cases. This good agreement between the FE simulations and the test results shows that the detailed FE model can capture the response of the welded H-beams under impact loadings.

Having gained confidence in the reliability of the detailed FE model, this is used in subsequent sections to investigate the development of the internal force and dissipated energy in comparison with the corresponding testing results, as depicted in Fig. 17 and Fig. 18, respectively. The development of internal force simulated by FE models will be described and discussed in details in Section 4.

In order to investigate the energy dissipation under the impact loading, the dissipated energy obtained from experiment and FE models was evaluated by calculating the area of impact force-rotation curves shown in Fig. 16 multiplied by half length of the beam. It can be seen from Fig. 17 that the dissipation ratio for all specimens is around 80%～90%. It is also observed from the comparison between experimental and FE results that reasonable estimates were obtained in all cases. The slight differences can be attributed to the idealized simulation of the friction between the hammer and the dropping rail as well as the boundary conditions of the beam supports.

4. Discussion of Catenary action

The main behavioural patterns and the key response characteristics including the development of impact force, deformation and strain, as well as failure modes were examined above through experimental and numerical investigation. This section further describes and discusses the development of internal force as well as catenary action for all the specimens.

Fig. 18 depicts the relationship of the moment and axial force at the mid-span section to the rotation obtained from experimental and numerical results for all specimens, where M_p and N_p was the plastic bending and axial capacity, respectively. The testing values of M and N were integrated by the derived stress corresponding to the testing strain in the mid-span section (including S1, S3, S5 and S2 as summarized in Fig.10), while numerical M and N were then adopted directly from the FE models.

It is evident from the experimental M-N curves in Fig. 18 that the beam axial force developed gradually after the beam yield due to the bending force. This can be further confirmed from the strain distribution of mid-span section at the rotation of 0.056 rad and 0.063 rad for Specimen HW11-56, and 0.078 rad and 0.095 rad for Specimen HW11-58 in Fig. 10, where the tension strain located at most of the mid-span section but with development of a little compression strain. As expected, the axial force may increase into its plastic value with the decreasing of the moment. To this end, the

internal force of the beam sections may be developed mostly from the axial force, which is known as catenary action. Due to the limited impact energy, the developed axial force of all specimens were lower than its plastic capacity as shown in Fig. 18, but the maximum rotation of the beam specimens was nearly close to 0.1 rad. It is shown that the welded H-beam was strong enough to develop catenary action. Furthermore, it is found that the development tendency of catenary action for the welded H-beams was consistent with the conclusion in other similar researches [5,10].

The interaction trend obtained from numerical simulations was similar to the testing results. The axial force developed gradually in the beam. This can be also confirmed from the FE deformation modes with stress nephogram in Fig. 19, as further discussed below.

Fig.19 depicts the distribution of Von Misses stress for Specimen HW11-56 at four significant stages. Herein, Specimen HW11-56 is taken as a typical example for a more detailed discussion on the development of catenary action. It is evidently observed from the identification of the key deformation stages that the development of catenary action was happening in the welded H-beam. At the impact instant, the maximum impact force was achieved as discussed from the testing results. Moreover, it is observed from the Von Misses stress distribution in Fig. 19(a) that the compression stress developed in the mid-span beam due to the inverted arch effect under suddenly applied impact load. It is demonstrated that a negative moment generated around the middle part of the welded

beam in the sudden impact, as the large impact forces were mainly undertook by the inertia of the structure before the forces reached the beam supports. Saatci and Vecchio [29] also performed an experimental programme on the reinforced concrete beam under impact loads, and the same conclusion was drawn that negative bending moment formed at the initial stage of impact response through experimental observation and theoretical analysis. After the peak impact force, the beam rebounded and worked normally like a static structure. Initially, the beam deformation remained elastic as shown in Fig. 19(b). Afterwards, a fluctuant descending impact force took place, but the beam bending moment grew rapidly in order to resist the impact energy. It is also stated from the deformation patterns and stress distribution in the mid-span beam in Fig. 19(c) that the plasticity occurred at this stage. When the impact force tended to be stable, the beam moment also kept unchanged. However, the tension force then raised gradually in the specimen. It can be clearly shown from Fig. 19(d) and (e) that the beam deformation shape was gradually close to catenary line, and the tension stress took over most of the beam middle sections. It is stated that the catenary mechanism took place at the welded H-beam.

Based on the testing and numerical result, it can be concluded that the internal force of beam changed from pure bending into combination of bending and axial force during the impact procedure. This development of the catenary action was clearly described and discussed in terms of both impact tests and FE models.

5. Conclusion

The dynamic behaviour and catenary action of axially restrained steel beam under impact loadings have been examined by means of experimental and numerical studies. An experimental program comprising six impact tests on the axially restrained welded H-beams has been described in details. The main behavioural patterns and the key response characteristics including the development of impact force, deformation and strain, as well as failure modes are examined.

It was shown that higher impact energy resulted in more obvious local buckling deformation, especially for the welded H-beams with larger width to thickness ratio. Importantly, it was noted that the influence of impact energy on the peak impact force and the development of the impact force can be negligible, but the larger impact energy results in higher impact duration. When the effect of width to thickness ratio was taken into account, beam deflection was proportionally related to the corresponding normalized impact energy. The increasing ratio of flange width to thickness remarkably deteriorated the impact resistance of steel beams. Moreover, it is shown that the beam load-carrying capacity was significantly improved when considering the effect of catenary action and dynamic effect.

Nonlinear finite element models have been also developed and calibrated against the experimental results. In general, the numerical estimations were found to correlate well with experimental results in beam deformation patterns as well as the development of

impact force. It is demonstrated that the detailed FE model can capture the response of the welded H-beams under impact loadings.

Furthermore, the mechanism of catenary action was also identified based on the development of the internal force for the welded H-beams through a combination of experimental and numerical investigation. It is shown that the development tendency of catenary action for the welded H-beams was consistent with the conclusion in other similar researches.

Acknowledgement

The financial support of National Natural Science Foundation for the project (51078139) research described in this paper is gratefully acknowledged. The authors would also like to thank the support of the Program for New Century Excellent Talents in University (NCET-11-0123). Additionally, the authors are grateful to the support with the experimental work at the Center for Integrated Protection Research of Engineering Structures (CIPRES), as well as Ministry of Education Key Laboratory of Building Safety and Efficiency in Hunan University.

Reference

[1] ASCE. Minimum Design Loads for Buildings and Other Structures. Reston, Virginia: American Society of Civil Engineers, 2005.

[2] Unified Facilities Criteria (UFC). Design of Buildings to Resist Progressive Collapse. 2005.

[3] National Institute of Standard and Technology (NIST). Best Practices for Reducing the Potential for Progressive Collapse in Buildings. 2007.

[4] Fu F. Progressive collapse analysis of high-rise building with 3-D finite element modeling method. Journal of Constructional Steel Research, 2009, 65(6): 1269-1278.

[5] Lee C, Kim S, Han K, et al. Simplified nonlinear progressive collapse analysis of welded steel moment frames. Journal of Constructional Steel Research, 2009, 65(5): 1130-1137.

[6] Yu M, Zha X X, Ye J Q. The influence of joints and composite floor slabs on effective tying of steel structures in preventing progressive collapse. Journal of Constructional Steel Research, 2010, 66(3): 442-451.

[7] Wang K Q, Li G Q, Yang T C. A study of restrained steel beams with catenary action under distributed load—Part I: theoretical model. China Civil Engineering Journal, 2010, 43(1): 1-7.

[8] Valipour HR, Bradford M. An efficient compound-element for potential progressive collapse analysis of steel frames with semi-rigid connections. Finite Elements in Analysis and Design, 2012, 60: 35-48.

[9] Izzuddin A, Vlassis AG, Elghazouli AY, Nethercot DA. Progressive collapse of

multi-storey buildings due to sudden column loss – part I: simplified assessment framework. Engineering Structure, 2008, 30:1308–18.

[10] Kim J, An D. Evaluation of progressive collapse potential of steel moment frames considering catenary action. The Structure Design of Tall and Special Buildings, 2009, 18(4): 455-465.

[11] Liu J L. Preventing progressive collapse through strengthening beam-to-column connection, Part 1: Theoretical analysis. Journal of Constructional Steel Research, 2010, 66 (2): 229-237.

[12] Liu J L. Preventing progressive collapse through strengthening beam-to-column connection, Part 2: Finite element analysis. Journal of Constructional Steel Research, 2010, 66(2): 238-247.

[13] He Q F, Yi W J. Experimental study of the collapse-resistant behavior of RC beam-column sub-structures considering catenary action. China Civil Engineering Journal, 2011, 44(4): 52-59.

[14] Sadek F, Main JA, Lew HS, Bao YH. Testing and analysis of steel and concrete beam-column assemblies under a column removal scenario. Journal of Structural Engineering, 2011, 137: 881-892.

[15] Huo J S, Zhang J Q, Chen B S, et al. Dynamic behaviours of hot-rolled steel bemas under drop weight impact loading. Journal of Building Structures, 2011, 32(12): 242-249.

[16] Li L, Wang W, Chen Y, Lu Y. Effect of beam web bolt arrangement on catenary behaviour of moment connections. Journal of Constructional Steel Research, 2015, 104: 22-36.

[17] GB50017—2003. Code for design of steel structures. Beijing: China Planning Press, 2003. (in Chinese))

[18] Jones N, Shen WQ. A theoretical study of the lateral impact of fully clamped pipelines. Proc Inst Mech Eng Part E J Process Mech Eng, 1992, Vol.206: 129-46.

[19] Fujikake K, Li B, Soeun S. Impact response of reinforced concrete beam and its analytical evaluation. Journal of Structure Engineer, 2009,135(8), 938-950.

[20] ABAQUS. ABAQUS theory manual, version 6.7. Hibbit. Karlsson and Sorensen. Inc.; 2003.

[21] Symonds P S. Survey of methods of analysis for plastic deformation of structures under dynamic loading. Brown University, Division of Engineering Report, BU/NSRDC, 1967, 1-67.

[22] Munoz-Garcia E, Davison J B, Tyas. An analysis of the response of structural bolts subjected to rapid rates of loading. In: Euro steel Conference on Steel and Composite Structures, Maastricht, The Netherlands, 2005.

[23] Johnson, G.R. and Cook, W.H. A constitutive model and data for metals subjected to large strains, high strain rates and high temperatures. Proceeding of the seventh International Symposium on Ballistics, The Netherlands Publishers, Hague, 1983,

541-547.

[24] Cowper, G.R. and Symonds, P.S. Strain hardening and strain-rate effects in the impact loading of cantilever beams. Brown University Division of Applied Mathematics Report No. 28, 1957.

[25] Izzuddin B A, Song L, Elnashi A S, Dowling P J. An integrated adaptive environment for fire and explosion analysis of steel frame, Part Ⅱ: Verification and application. Journal of Constructional Steel Research, 2000, 53(1): 87-111.

[26] Liew R, Chen H. Inelastic transient analysis of steel frame subjected to explosion and fire. Department of Civil Engineering, National University of Singapore. 2002.

[27] Chen H, Liew R. Explosion and fire analysis of steel frame using mixed element approach. Journal of Engineering Mechanics, 2005, 131(6): 606-616.

[28] Jones, N. Structural Impact, Cambridge University Press, Cambridge,1989, 411-441.

[29] Saatci S and Vecchio FJ. Effects of shear mechanisms on impact behavior of reinforced concrete beams. ACI Structure Journal, 2009, 106(1): 78-86.

Figures

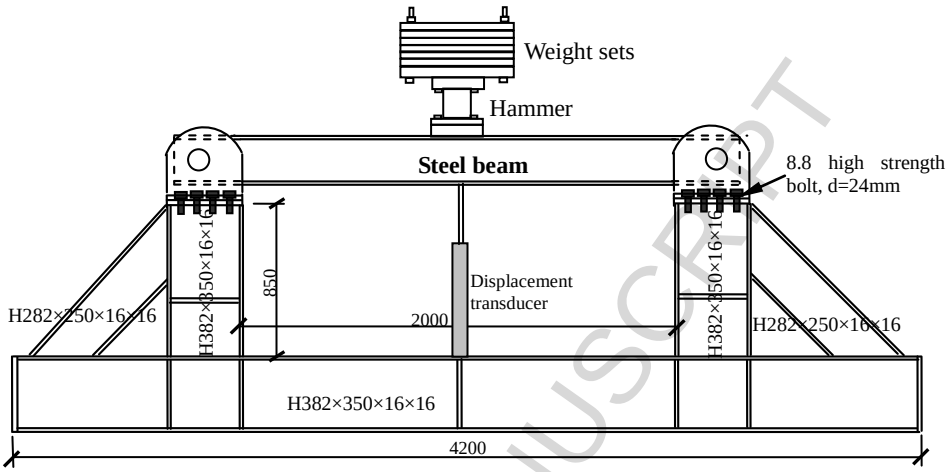

(a) Schematic representation

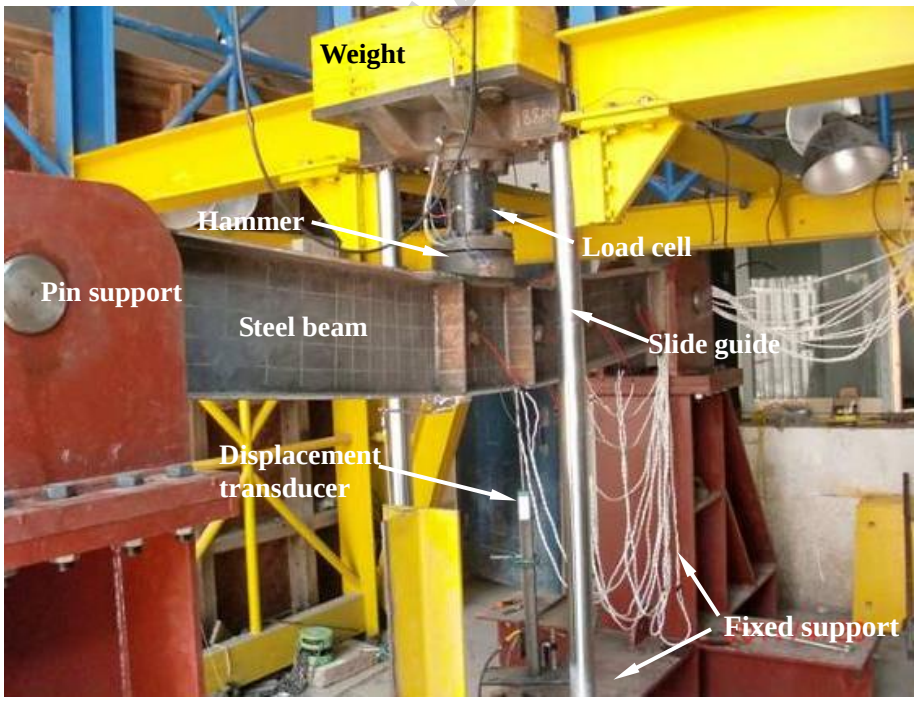

(b) General view of impact test

Fig. 1 Impact test setup for axially restrained steel beam (Unit: mm)

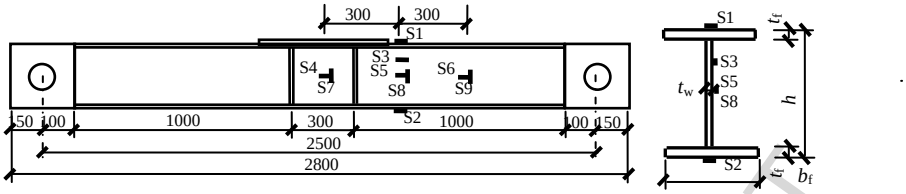

Fig. 2 Details of restrained steel beam and location of the strain gauges

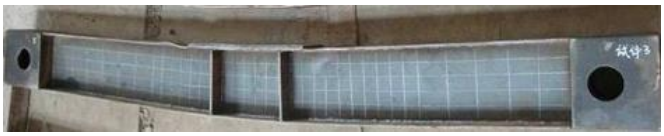

(a) Specimen HW9-45

(b) Specimen HW9-56

(c) Specimen HW11-56

(d) Specimen HW11-58

(e) Specimen HW14-58

(f) Specimen HW14-77

Fig. 3 Deformation modes for the welded H-beams at the end of the impact tests

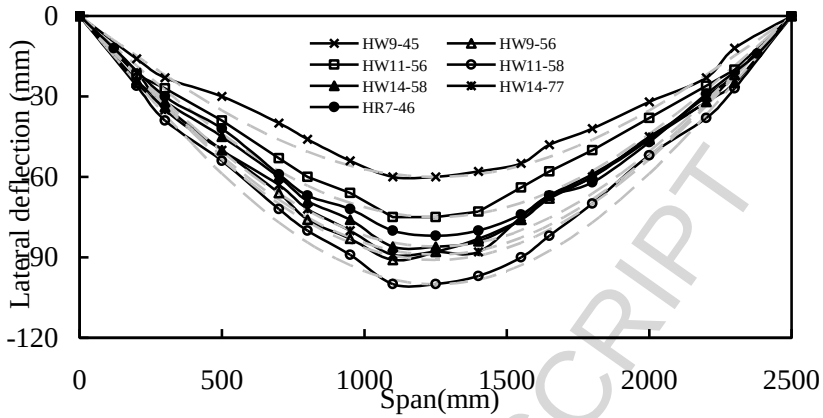

Fig. 4 Beam residual deflection shapes in comparison with the half-sinusoid curves

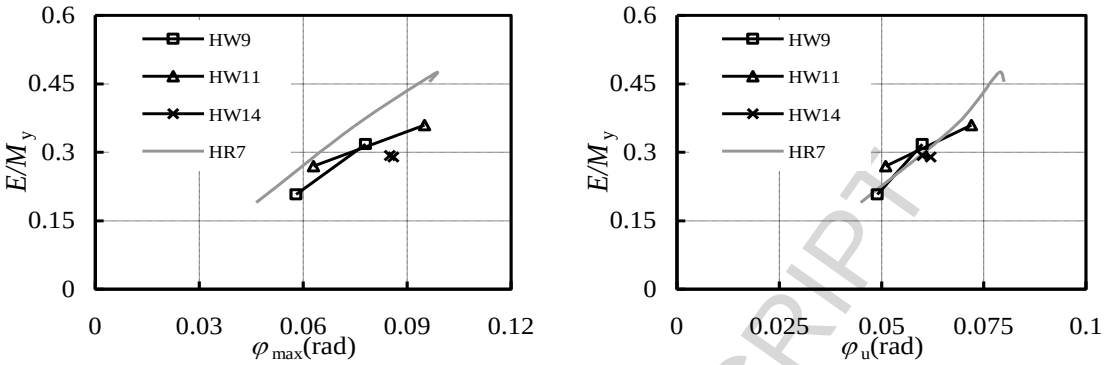

(a) Maximum rotation (b) Residual rotation

Fig.5 Normalized impact energy-beam rotation curves for all specimens divided by width-thickness ratio

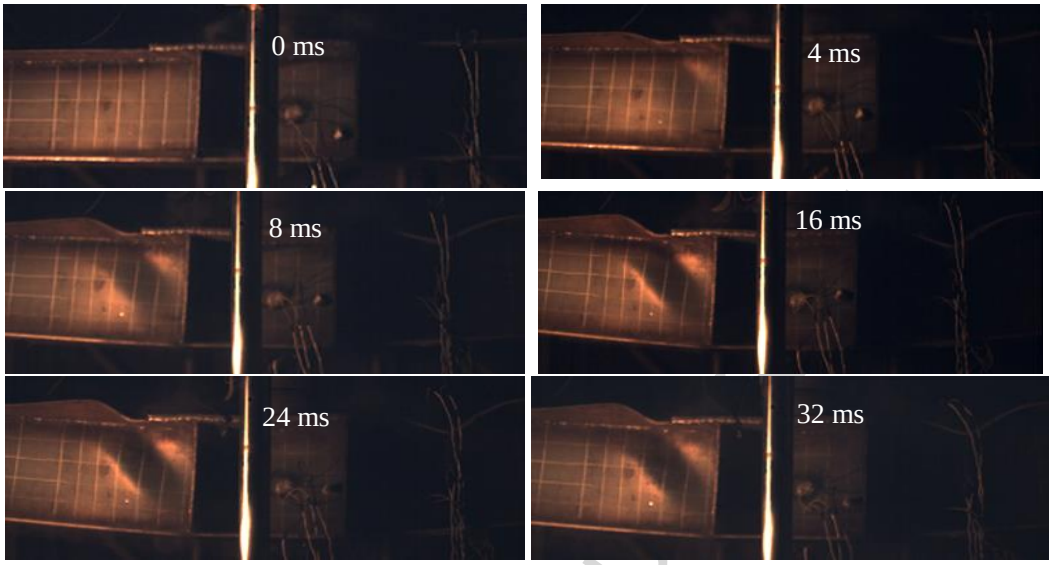

Fig. 6 Deformation development for Specimen HW14-76 from 0 ms to 32 ms

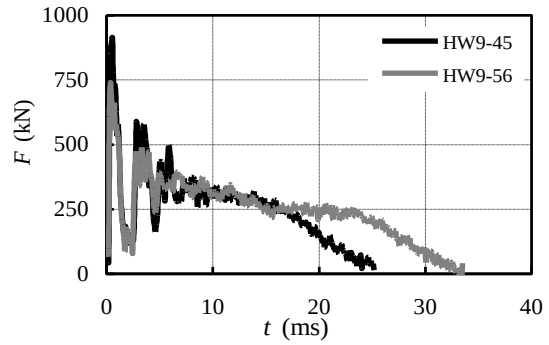

(a) λ=9

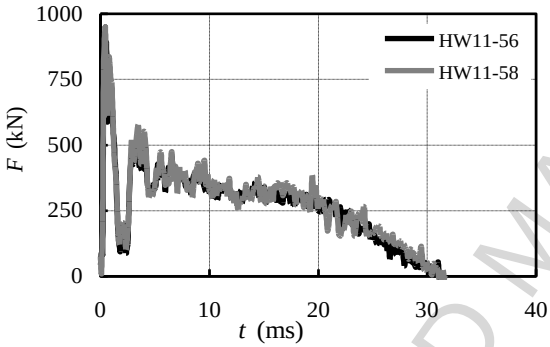

(b) λ=11

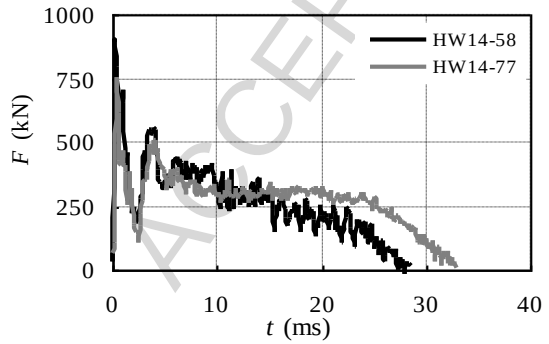

(c) λ=14

Fig. 7 Time history curves of impact force for all specimens

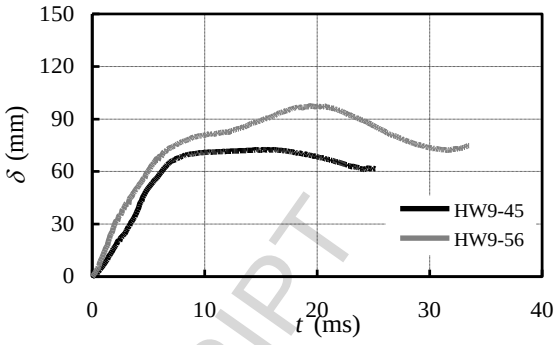

(a) λ=9

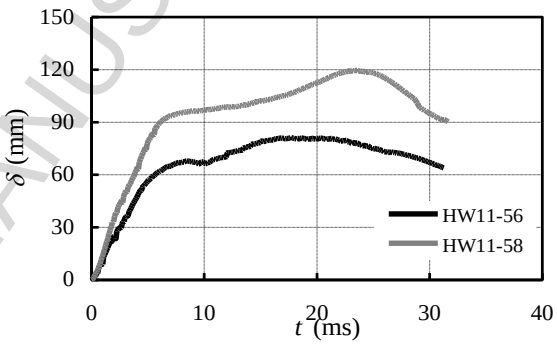

(b) λ=11

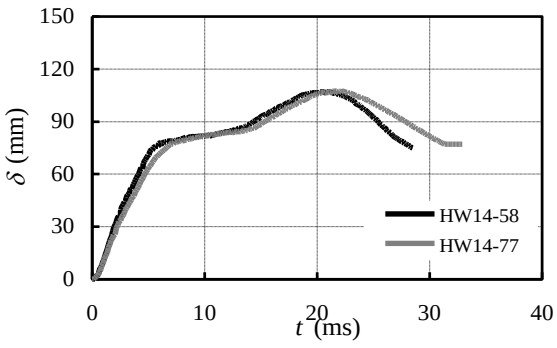

(c) λ=14

Fig. 8 Time history curves of the mid-span displacement for all specimens

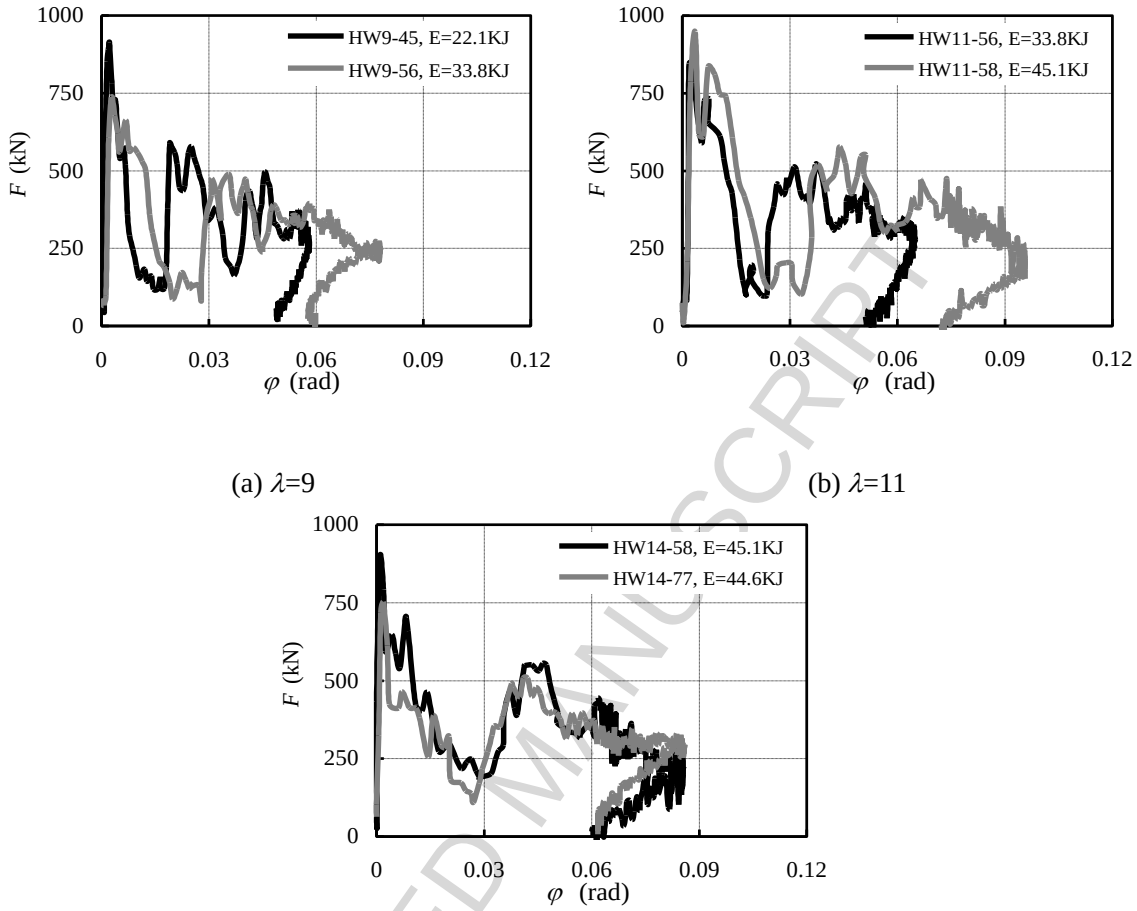

(a) λ=9 (b) λ=11

(c) λ=14

Fig. 9 Impact force-rotation relationship for all specimens

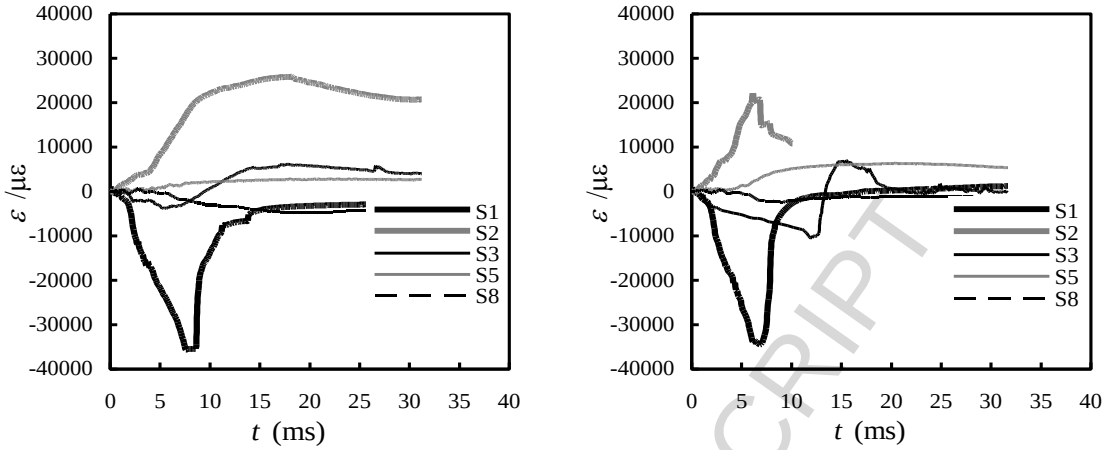

(a) Specimen HW11-56

(b) Specimen HW11-58

Fig.10 Strain versus time relations of restrained steel beams

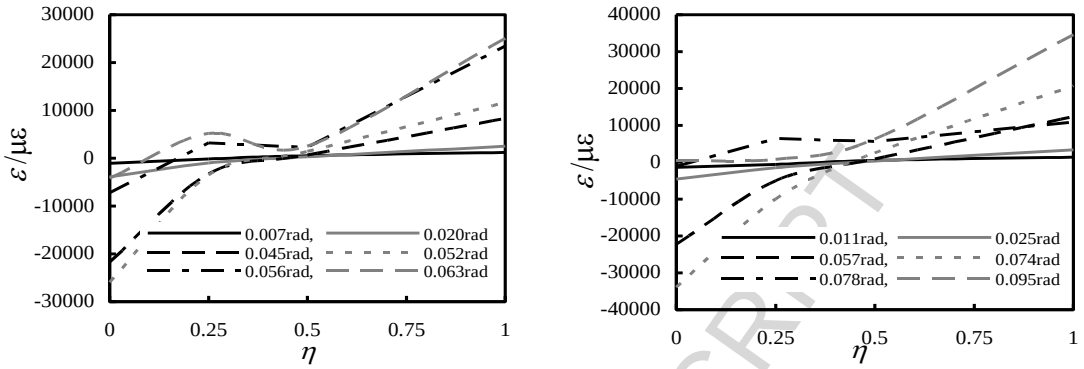

(a) Specimen HW11-56 (b) Specimen HW11-58

Fig.11 Strain development of mid-span section at different impact stages

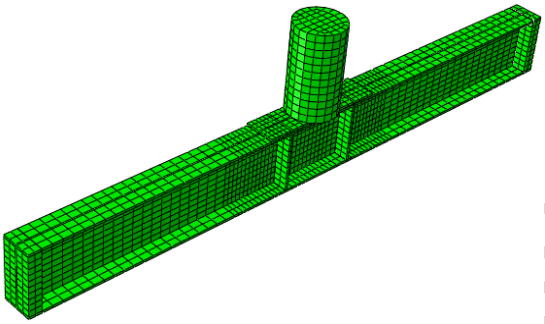

Fig.12 View of the finite element model

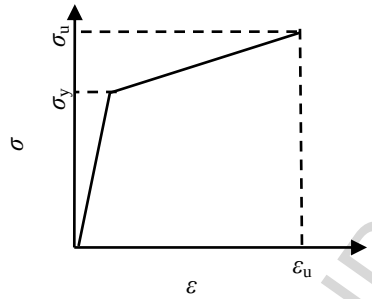

Fig. 13 Linear hardening model for steel material

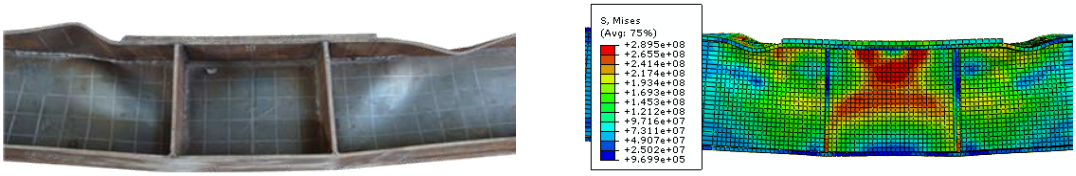

Experiment Numerical model

(a) Specimen HW9-56

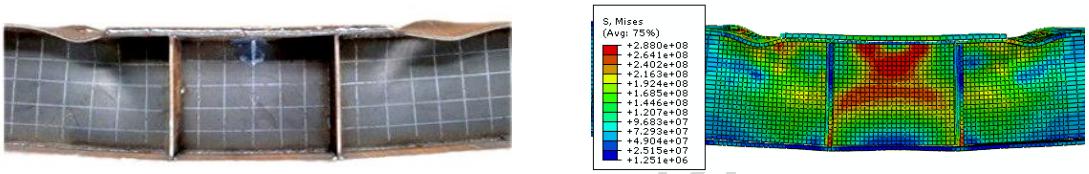

Experiment Numerical

(b) Specimen HW11-56

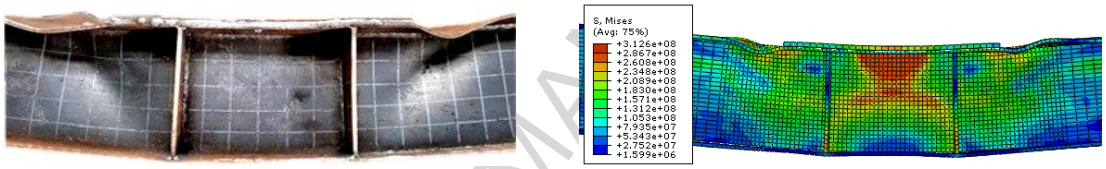

Experiment Numerical

(c) Specimen HW11-58

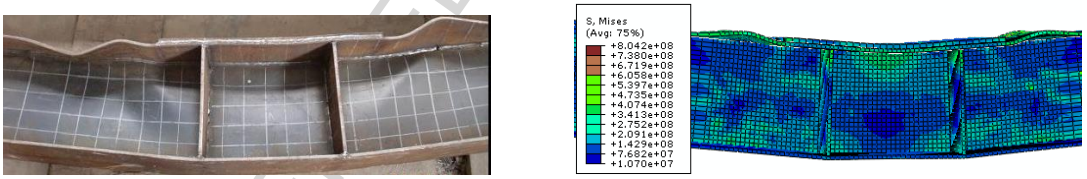

(d) Specimen HW14-58

Fig. 14 Comparisons of deformation patterns from experiment and FE models at the beam mid-span zone

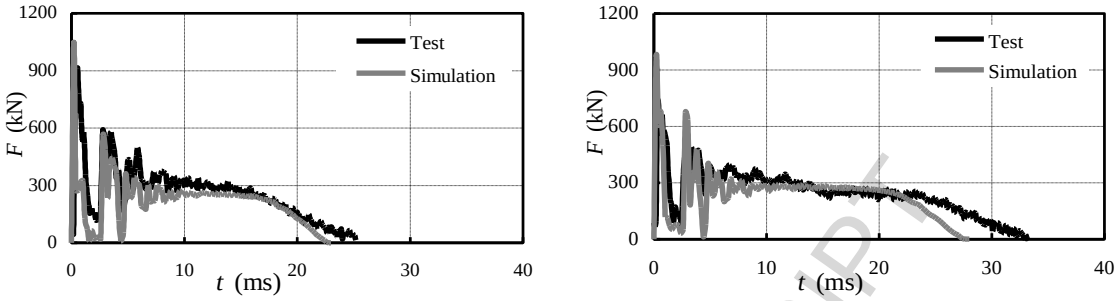

(a) Specimen HW9-45

(b) Specimen HW9-56

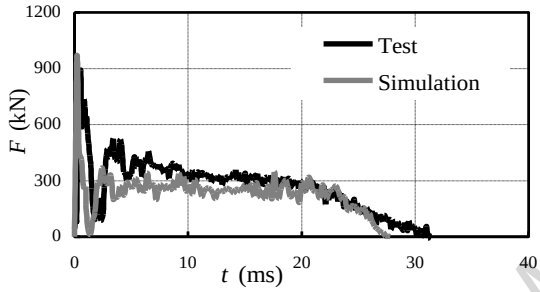

(c) Specimen HW11-56

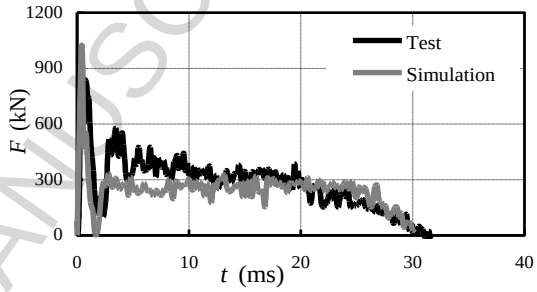

(d) Specimen HW11-58

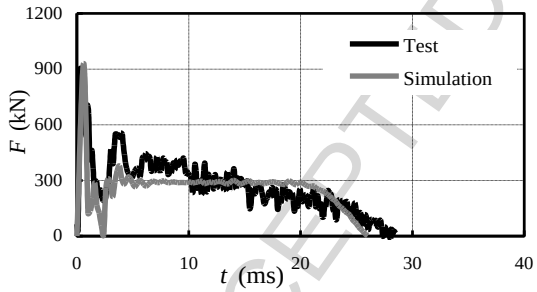

(e) Specimen HW14-58

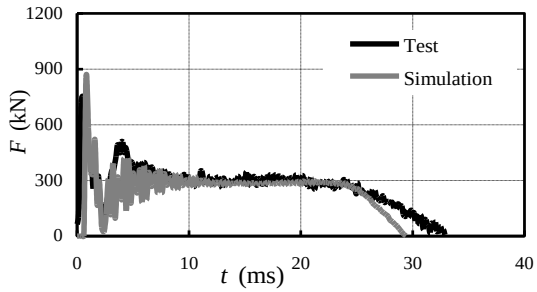

(f) Specimen HW14-77

Fig. 15 Comparison of experimental and predicted impact force-time relationships for all specimens

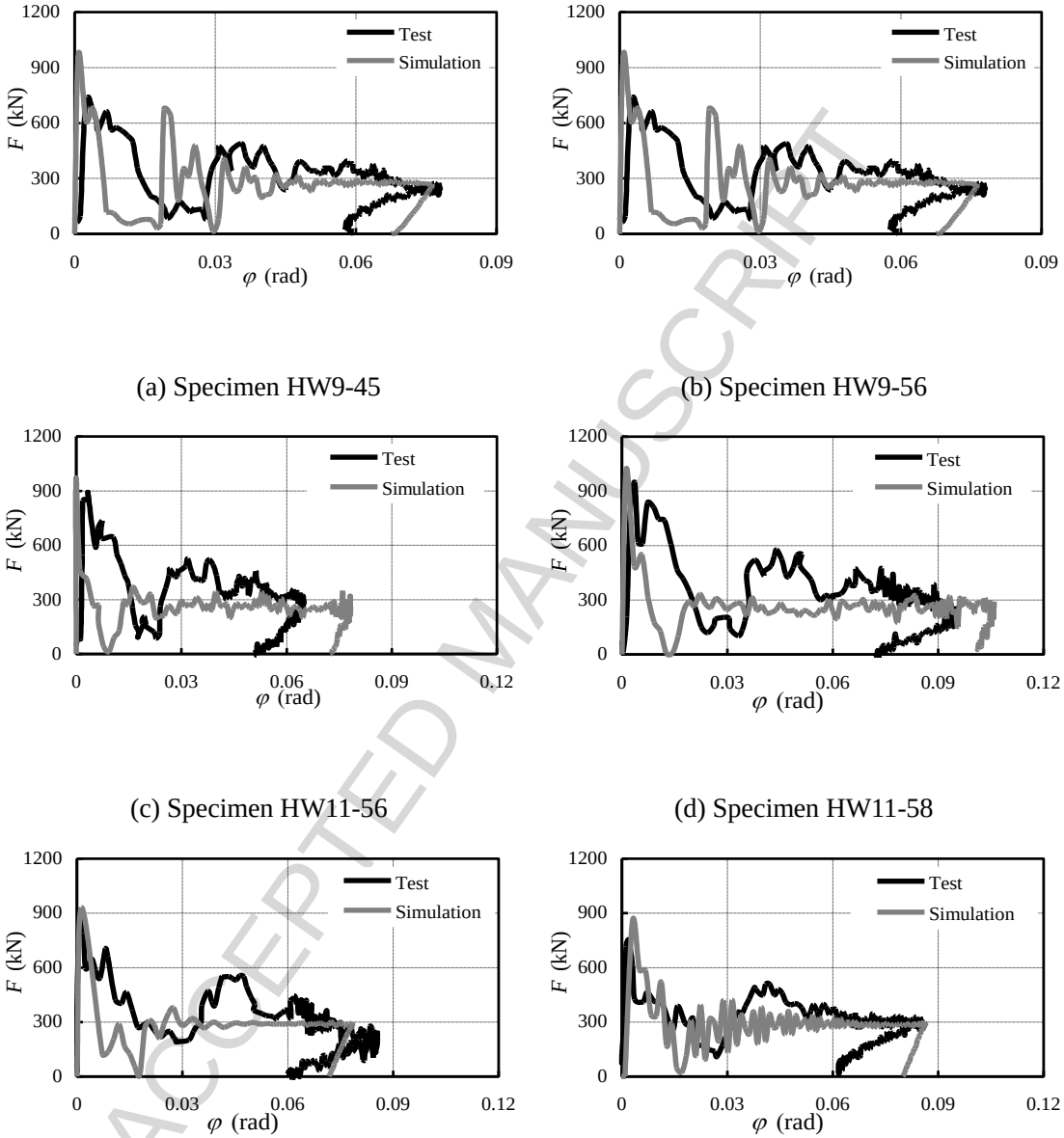

(a) Specimen HW9-45

(b) Specimen HW9-56

(c) Specimen HW11-56

(d) Specimen HW11-58

(e) Specimen HW14-58

(f) Specimen HW14-77

Fig.16 Comparison of experimental and predicted impact force-rotation relationships for all specimens

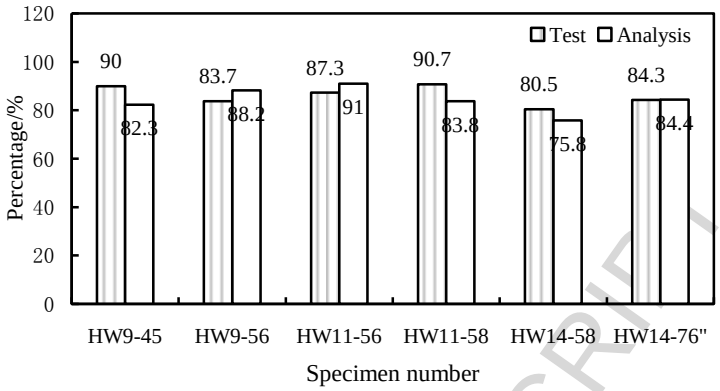

Fig.17 Comparison of ratio between dissipated energy and applied impact energy from experiment and FE models for all specimens

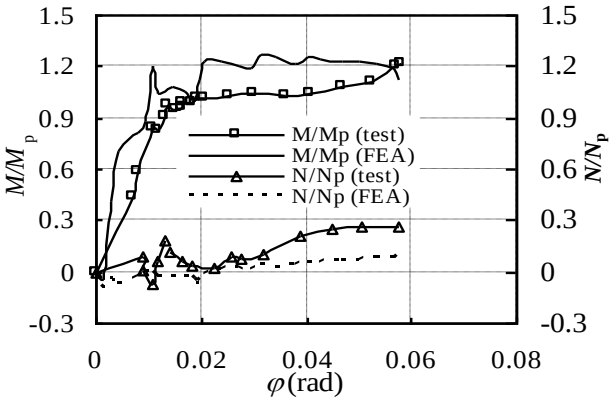

(a) HW9-45

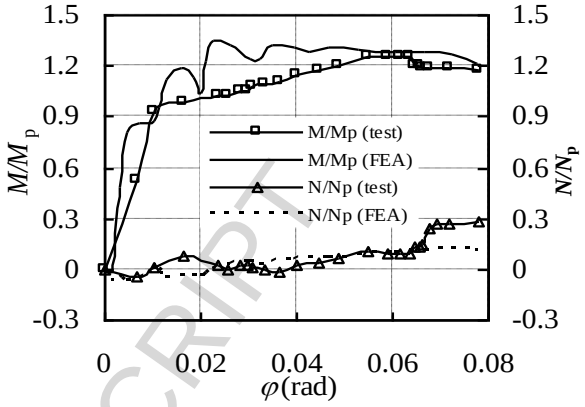

(b) HW9-56

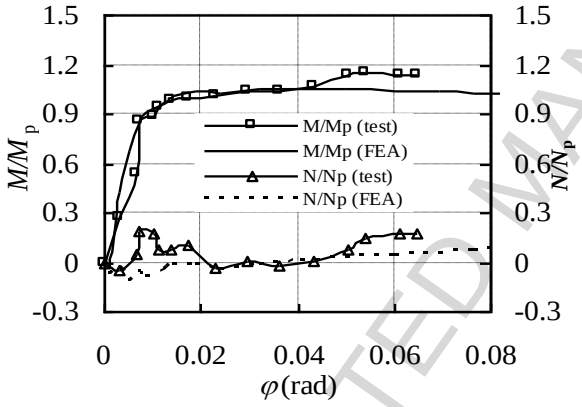

(c) HW11-56

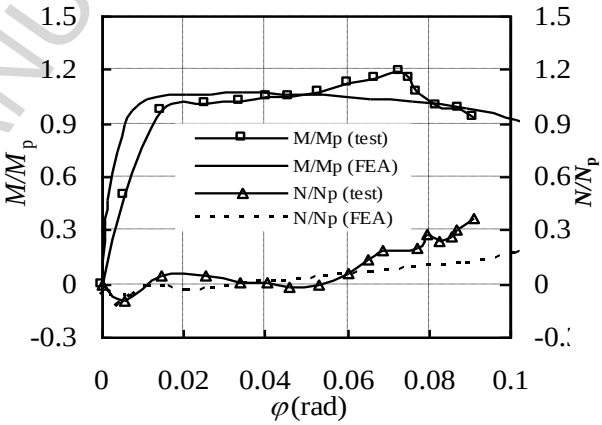

(d) HW11-58

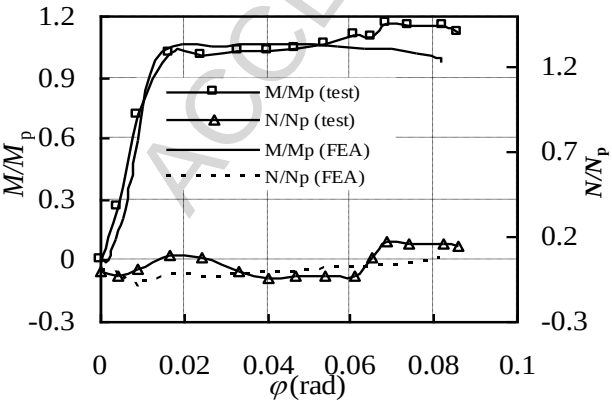

(e) HW14-58

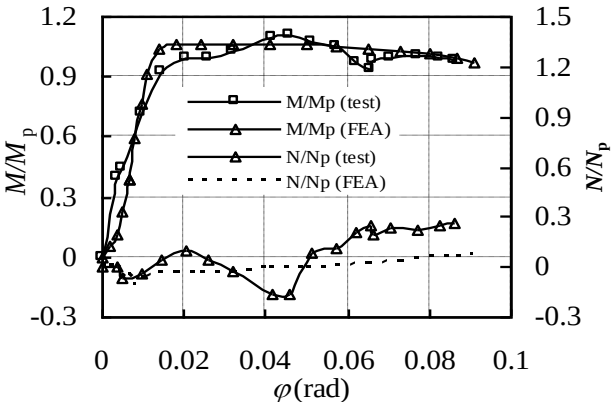

(f) HW14-77

Fig. 18 Moment versus rotation and axial load versus rotation relations of restrained steel beams

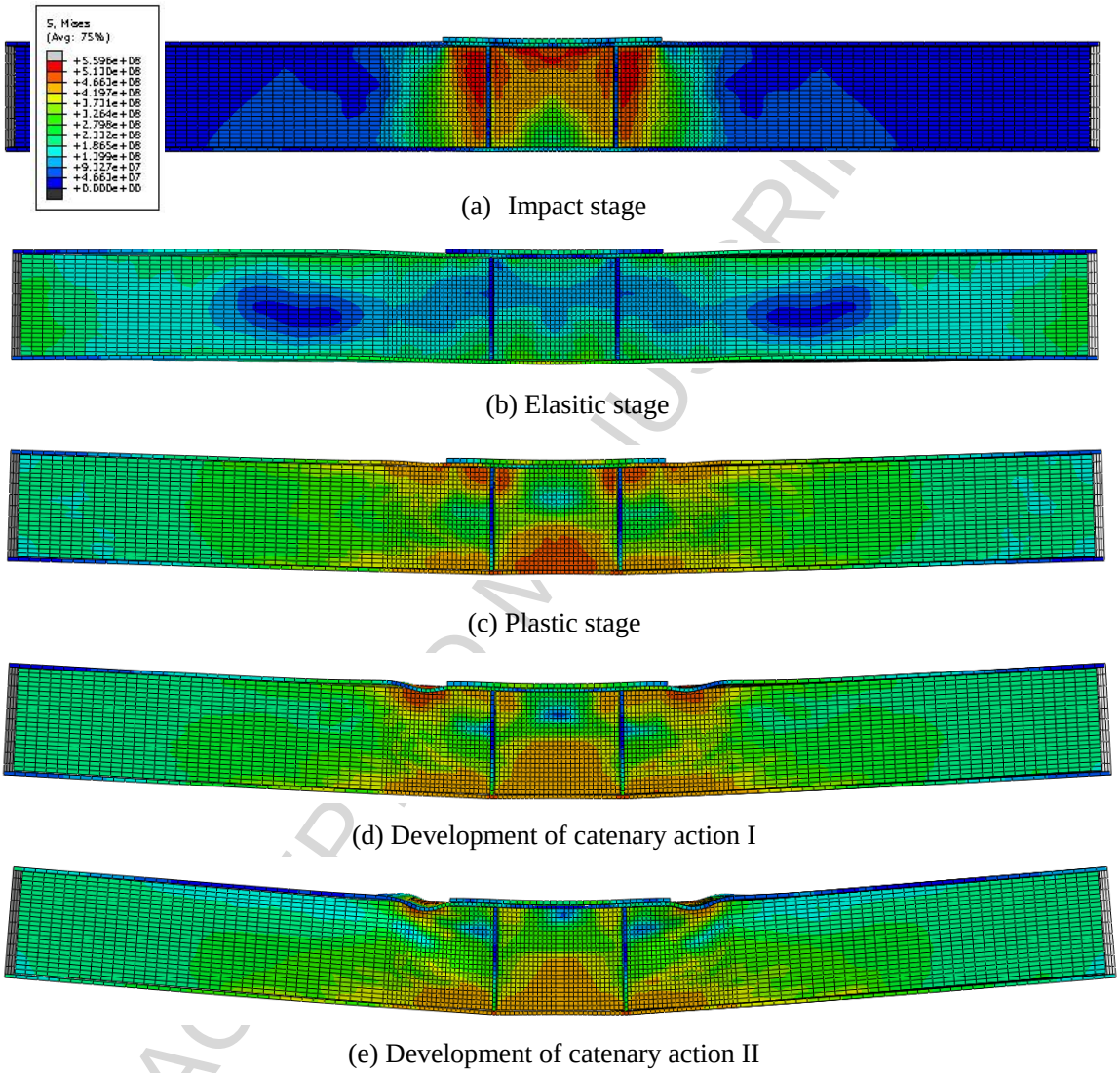

(a) Impact stage

(b) Elasitic stage

(c) Plastic stage

(d) Development of catenary action I

(e) Development of catenary action II

Fig. 19 Distribution of Von Misses stress for Specimen HW11-56 under impact load

Tables

Table 1 Details of testing specimens

Reference	$h\times b_f\times t_w\times t_f$ (mm)	λ	M (kg)	v (m·s^{-1})	E_1 (kJ)	E_1/M_y (J·m/N)	$F_{u,max}$ (kN)	$F_{u,e}$ (kN)	$F_{u,c}$ (kN)	F_p (kN)	φ_{max} (rad)	φ_u (rad)	E_2 (kJ)	$\dot{\varepsilon}$	DAF_1 ($F_{u,c}/F_p$)	DAF_2 ($F_{u,e}/F_{u,c}$)	DAF_3 (F_u/F_p)
Welded H-beams																	
HW9-45	H266×150×6×8	9.0	450	10.0	22.1	0.21	860	325	244	190	0.058	0.0499	19.3	2.18	1.28	1.33	1.71
HW9-56			575	10.8	33.8	0.32	747	350	245	190	0.078	0.0603	28.3	5.30	1.29	1.43	1.84
HW11-56	H266×182×6×8	11.0	575	10.8	33.8	0.27	880	374	267	230	0.063	0.0515	29.5	4.43	1.16	1.40	1.63
HW11-58			575	12.5	45.1	0.36	822	382	290	230	0.095	0.0729	40.9	4.90	1.26	1.32	1.66
HW14-58	H266×230×6×8	14.0	575	12.5	45.1	0.29	863	382	281	270	0.085	0.0603	36.3	5.45	1.04	1.36	1.41
HW14-77			700	11.3	44.6	0.29	765	355	290	270	0.086	0.0626	37.6	5.20	1.07	1.22	1.31
Hot-rolled H-beams (Huo et al. [15])																	
HR7-43	H250×125×6×9	7.0	450	7.9	14.1	0.19	847	219	168	136	0.0046	0.0449	12.6	2.32	1.24	1.30	1.61
HR7-46	H250×125×6×9		450	10.8	26.5	0.36	790	260	176	136	0.0075	0.0678	23.3	3.93	1.29	1.48	1.91
HR7-48	H250×125×6×9		450	12.5	35.3	0.47	819	245	177	136	0.0098	0.0786	29.8	5.17	1.30	1.38	1.80
HR7-56	H250×125×6×9		575	10.8	33.8	0.45	627	278	190	136	0.0096	0.08	30.6	4.84	1.40	1.46	2.04

Note: In the reference, HW and HR stand for welded and hot-rolled H shape sections, followed by the width-thickness ratio, the weight of the hammer (where the number '4' '5' '7' stands for 450 kg, 575 kg and 700 kg, respectively), as well as the dropping height (where the number '5' '6' '8' '7' stands for 5.0 m, 6.0 m, 8.0 m and 6.5 m, respectively. λ is the width thickness ratio (b_f/t_f). M and v are the mass and the velocity of the testing hammer, respectively.

Table 2 Static material properties of welded H-beam components

Components	f_{ys}(MPa)	f_u(MPa)	f_u/f_{ys}	Elongation rate %	E_s (MPa)
HW web	267.8	386.7	1.44	20.7	1.78×10^5
HW flange	296.7	440.5	1.48	21.3	1.81×10^5